# The growth of hematite nanobelts and nanowires—tune the shape via oxygen gas pressure

Lu Yuan
*Department of Mechanical Engineering and Multidisciplinary Program in Materials Science and Engineering, State University of New York, Binghamton, New York 13902*

Qike Jiang and Jianbo Wang
*School of Physics, Center for Electron Microscopy and Ministry of Education Key Laboratory of Artificial Micro- and Nano-Structures, Wuhan University, Wuhan 430072, China*

Guangwen Zhou[a]
*Department of Mechanical Engineering and Multidisciplinary Program in Materials Science and Engineering, State University of New York, Binghamton, New York 13902*

Using the thermal oxidation of iron, we show that the growth morphologies of one-dimensional nanostructures of hematite ($\alpha$-Fe$_2$O$_3$) can be tuned by varying the oxygen gas pressure. It is found that the oxidation at the oxygen gas pressures of ~0.1 Torr is dominated by the growth of hematite nanobelts, whereas oxidation at pressure near 200 Torr is dominated by the growth of hematite nanowires. Detailed transmission electron microscopy study shows that both the nanobelts and nanowires grow along the [11$\bar{2}$0] direction with a bicrystal structure. It is shown that nanowires are rooted on Fe$_2$O$_3$ grains, whereas nanobelts are originated from the boundaries of Fe$_2$O$_3$ grains. Our results show that oxygen gas pressure can be used to manipulate the Fe$_2$O$_3$/Fe$_3$O$_4$ interfacial reaction, thereby tailoring the oxide growth morphologies via the stress-driven diffusion.

## I. INTRODUCTION

Tailoring the shape of nanostructures is one of the key challenges in the growth control. It has been shown that the growth morphologies of nanostructures can be changed by various mechanisms, e.g., via epitaxial stress for the growth of lattice-mismatched materials systems such as Ge/Si, InAs/InP, or using small-sized catalysts for the nanowire growth via a vapor–liquid–solid (VLS) mechanism.[1–9] Whereas VLS is the widely used mechanism for controlled growth of nanowires, the geometrical shapes (i.e., cross sections) of the resulting one-dimensional structure are usually defined by energetics, and shape-dependent thermodynamic models based on a geometric summation of the Gibbs free energies of different crystal facets as a function of total volume and aspect ratio are usually adopted.[10–12] The growth of oxide nanowires by thermal oxidation of metals has recently received intensive interest, largely due to its technical simplicity and large-scale growth capabilities.[13–23] However, the precise mechanism underlying the one-dimensional oxide growth is still a matter of debate, and various models are proposed including the evaporation and condensation mechanism, i.e., vapor–solid

model,[13,24,25] short circuit diffusion mechanism (i.e., diffusion along a tunnel centered along the core of a screw dislocation),[26–28] and stress-driven diffusion.[29–31] Even less is known about the control in the growth morphologies of oxide nanowires during the oxidation process. This complexity is largely due to the convolution and coupling of different processes involved in the oxidation leading to the oxide nanowire formation, including layered oxide growth, interfacial reactions, mass transport, and stress generation and relaxation.

Hematite ($\alpha$-Fe$_2$O$_3$) is the most stable iron oxide. One-dimensional $\alpha$-Fe$_2$O$_3$ is a promising nanomaterial for advanced applications in catalysis, gas sensors, water splitting, dye solar cells, magnetic storage media, environmental protection, pigment, and controlled drug delivery.[32–37] $\alpha$-Fe$_2$O$_3$ nanowires have been obtained by various methods including templates,[38] sol-gel-mediated reaction,[39,40] solvothermal conditions,[41] and gas decomposition.[42] Although much effort is being given to develop nanoscale hematite by oxidation of iron,[20,43–48] the growth processes critical to the control in the growth morphology of nanoscale hematite during the thermal oxidation are still far from established. In this work, we show that the growth of either $\alpha$-Fe$_2$O$_3$ nanobelts or nanowires can be tuned via control of the oxygen gas pressure during the oxidation of iron. In contrast to the thermodynamically controlled growth shapes of one-dimensional nanostructures,[10–12] we find that the growth morphologies

of hematite, i.e., nanowires and nanobelts, are defined by the geometry and shape of the locations at which the nucleation and growth of nanowires and nanobelts occur. The results provide fundamental insight into understanding the interplay between the generation/relaxation of internal stresses, mass transport, and oxide growth morphologies during multi-phase layered oxide scale growth.

## II. EXPERIMENT

The oxidation experiment consists of a substrate heater located in the center of a vacuum chamber and a gas handling system. The temperature of the samples can be monitored by a K-type thermocouple connected with the heater. Fresh iron foils with 99.99% purity (Sigma-Aldrich, Missouri, MO) were used as the substrate for oxidation. The iron foils were first cleaned in deionized water followed by ultrasonication in ethanol for 5 min before putting on the substrate heater. Before oxidation, the system was sealed and pumped to a base pressure of $2 \times 10^{-6}$ Torr. High purity oxygen gas ($>99.99\%$) was introduced into the vacuum chamber to desired oxygen pressures ($pO_2$), and the samples were then heated at the rate of 20 °C/min to 600 °C. The oxygen gas pressure in the chamber was kept constant during the oxidation. After the oxidation at 600 °C, the samples were cooled down naturally (about 10 °C/min) to room temperature ($\sim$25 °C) under the same oxygen atmosphere. The oxidized samples were examined by field emission scanning electron microscopy (FE-SEM) (FEI Supra 55VP, Hillsboro, OR) and x-ray diffraction (XRD) (PANalytical, Westborough, MA). The growth morphology and atomic structure of individual nanowires and nanobelts were analyzed by transmission electron microscopy (TEM) using a JEOL JEM-2010-HT (Tokyo, Japan) operated at 200 kV.

## III. RESULTS

Our SEM observations reveal that the oxidized Fe surface is dominated by the growth of nanobelts for oxygen pressures around 0.1 Torr and by nanowire formation for oxygen pressures around 200 Torr. The growth of both nanowires and nanobelts occurs for the oxygen pressure values between the two oxygen pressure limits as above. Figure 1 shows representative SEM images of the Fe substrates oxidized for 1 h at T = 600 °C for the different oxygen gas pressures. Figure 1(a)–1(c) and Fig. 1(d)–1(f) are side view and top view SEM images, respectively, of the Fe substrates oxidized at $pO_2 = 0.1$, 50, and 200 Torr, respectively. For the oxidation at $pO_2 = 0.1$ Torr, it can be seen that the oxidized surface is covered by a high density of nanobelts with the width varying from 100 to 300 nm and length up to $\sim$5 μm. It is also noted that the width of nanobelts decreases along their length direction from the root to the tip. For the

oxidation at $pO_2 = 200$ Torr, the oxidized surface is covered by a high density of nanowires with the diameter ranging from 50 to 150 nm and length up to 6 μm. Nanowires show relatively uniform diameter along the length direction with a tapered shape at the tip. For the oxidation at $pO_2 = 50$ Torr, the substrate surface is covered by a mixture of nanobelts and nanowires, as shown in Fig. 1(b) and 1(e). The side view SEM images show that both nanobelts and nanowires are perpendicular to the substrate surfaces at their roots. No significant differences in lengths are found for nanowires and nanobelts formed under the different oxygen gas pressures. Figure 1(g)–1(i) shows the XRD results of the Fe substrates under the corresponding oxygen gas pressures. These XRD patterns match well with rhombohedral α-$Fe_2O_3$. The comparison to the standard polycrystalline α-$Fe_2O_3$ XRD pattern shows that the diffraction peak $(11\bar{2}0)$ exhibits much stronger intensity in these patterns, suggesting that both nanobelts and nanowires grow preferentially along $[11\bar{2}0]$ direction.

To obtain more quantitative information regarding the effect of oxygen pressure on the different oxide growth morphologies, more samples were oxidized at different oxygen pressures. Figure 2(a) shows the evolution of surface density of nanobelts and nanowires obtained from oxidation under different oxygen gas pressures, which reveals clearly that the surface density of nanobelts decreases with increasing oxygen gas pressure, whereas the surface density of nanowires increases with increasing the oxygen pressure. Figure 2(b) shows the evolution of proportion of nanobelts to nanowires as related to change in oxygen pressure. As can be seen, the oxygen gas pressure can tune efficiently the percentage of nanowires and nanobelts on the oxidized surface. In addition, we also examined the effect of oxidation temperatures ranging from 350 to 700 °C at the oxygen pressure of 200 Torr and noted that only nanowires are formed for these temperatures, suggesting relatively insignificant effect of the oxidation temperature on the oxide growth morphologies at constant oxygen gas pressure.

The effect of oxidation time on the oxide growth was also examined. We find that increasing the oxidation time results in longer and denser nanowires or nanobelts but no noticeable changes occur to the oxide morphologies under the particular oxygen gas pressure. This suggests that the shape of nanobelts or nanowires is defined in their initial formation stages and the shape is retained during the subsequent growth stages. Figure 3(a) and 3(b) are SEM images showing the initially formed nanowires and nanobelts on Fe substrates oxidized for only 30 min with $pO_2 = 0.1$ Torr and 10 min with $pO_2 = 200$ Torr, respectively. The SEM images reveal that both surfaces are covered with a layer of α-$Fe_2O_3$ oxide grains, and it can be seen that nanobelts and nanowires originate from different surface regions, i.e., nanobelts are associated with the grain boundary areas, whereas nanowires are formed directly on top of grains. Side view SEM images
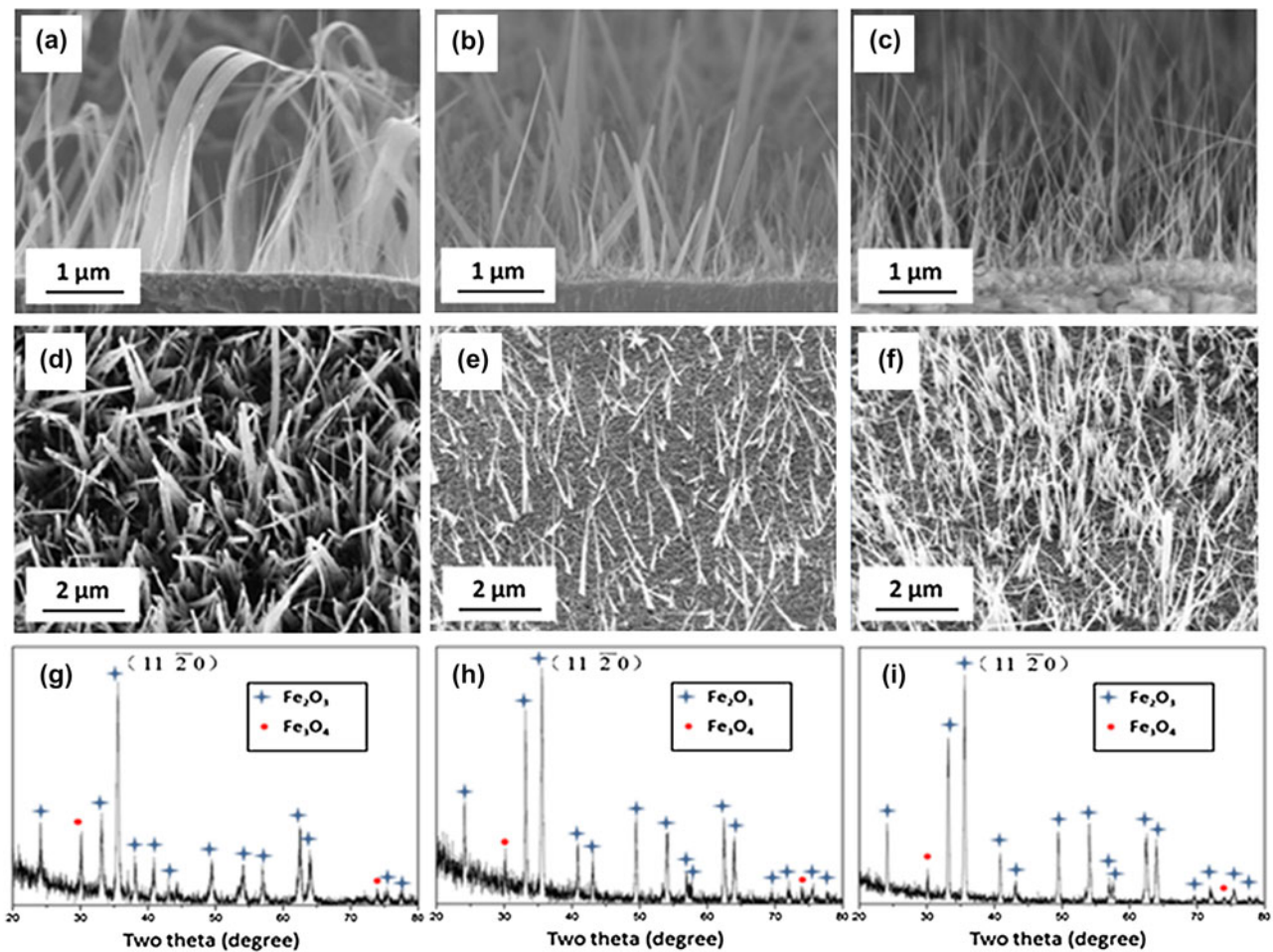
FIG. 1. SEM micrographs of the surface morphology of Fe foils oxidized at 600 °C for 1h under different oxygen gas pressures: Upper panel: side-view SEM images of Fe foils oxidized at (a) $pO_2 = 0.1$ Torr, (b) $pO_2 = 50$ Torr (b), and (c) $pO_2 = 200$ Torr; Middle panel: top-view SEM images (d, e, and f) of the Fe foils oxidized at the corresponding oxygen pressures; Lower panel: X-ray diffraction from the oxidized Fe foils for the different oxygen gas pressure [(g): $pO_2 = 0.1$ Torr, (h): $pO_2 = 50$ Torr, (i): $pO_2 = 200$ Torr].
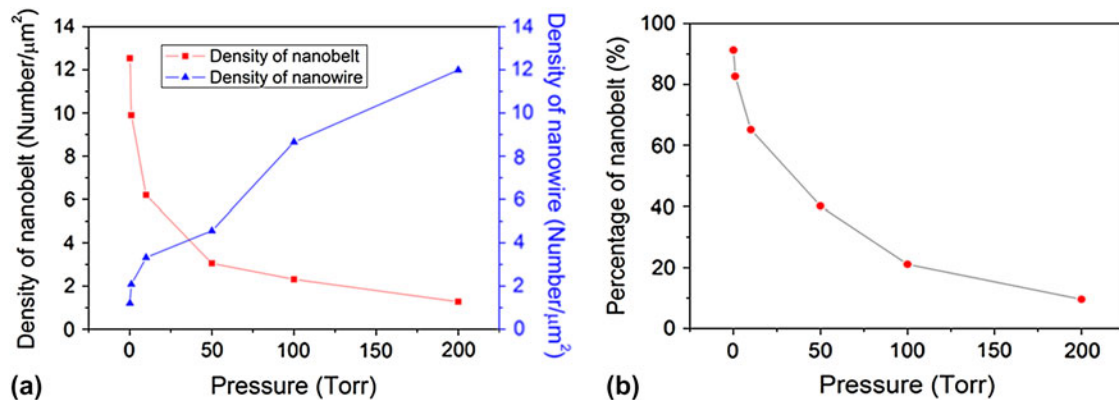


FIG. 2. (a) The surface density of the nanobelts and nanowires as a function of oxygen gas pressure; (b) the percentage of nanowires in the mixture of nanowires and nanobelts as a function of oxygen gas pressure.

[Fig. 3(c) and 3(d)] obtained from the oxidized samples confirm these growth features. It becomes clear from these observations that nanobelts grow out of grain boundaries, and the resulting morphology (wide in width but thin in thickness) is defined by the geometry of grain boundaries, i.e., wide and thin along the boundary, and nanowires grow on the top of grains and the resulting shape is correlated with the shape of grains.
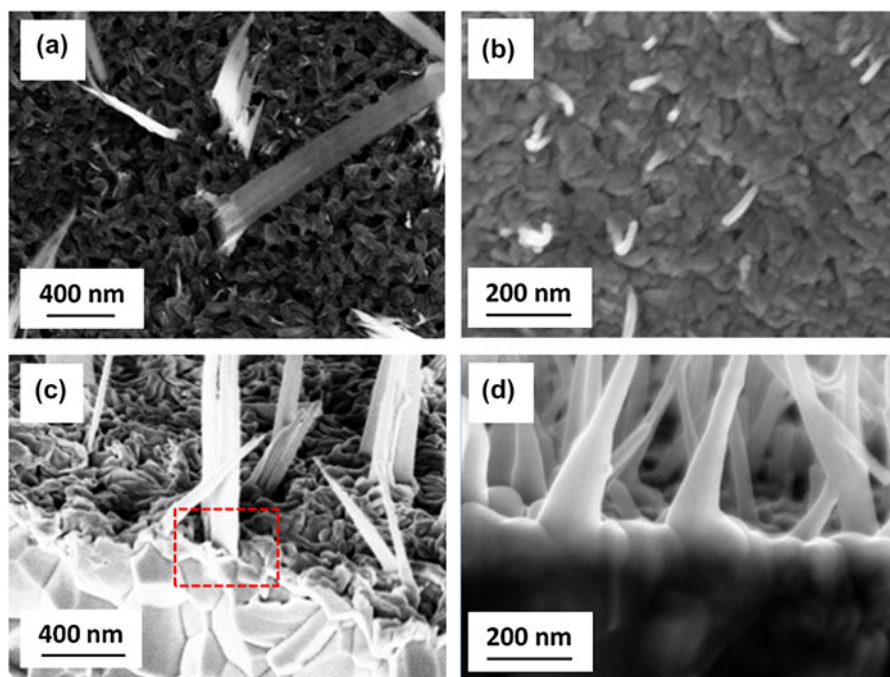
FIG. 3. The initial growth morphologies of nanobelts and nanowires: Upper panel: top views of Fe foils oxidized for 30 min at $pO_2 = 0.1$ Torr (a) and oxidized for 10 min at $pO_2 = 200$ Torr (b); lower panel: side-view SEM micrographs showing the root regions of nanobelts and nanowires obtained from the oxygen pressures of 0.1 Torr (c) and 200 Torr (d), the area indicated by the dashed box in (c) shows clearly that the nanobelt is grown out of the grain boundary.

The microstructures of nanobelts and nanowires were further examined by TEM. Figure 4(a) shows a bright-field (BF) TEM image of a typical nanobelt with a width of $\sim 200$ nm. Figure 4(b) is a selected area electron diffraction (SAED) pattern from the nanobelt. The diffraction pattern can be indexed with two sets of diffraction spots, one refers to an incident electron beam parallel to the [0001] zone axis and the other is the $[\bar{1}101]$ zone axis with $[0001]//[\bar{1}101]$. The appearance of the two sets of diffraction patterns from the same area suggests that the nanobelt has a bicrystal structure. In addition, by combining the morphology image and diffraction pattern in Fig. 4(a) and 4(b), we can find that the length direction of the nanobelt is along $[11\bar{2}0]$. Figure 4(c) and 4(d) displays a high-resolution transmission electron microscopy (HRTEM) image of the nanobelt and the corresponding Fourier transform pattern, which can be indexed in the same way as the diffraction pattern in Fig. 4(b), further confirming the bicrystal structure of the nanobelt. Note that the bicrystal boundary is not visible in the HRTEM image because the bicrystal plane is perpendicular to the incident electron beam.

Figure 5(a) shows a BF TEM image of a nanowire obtained from the oxidation at $pO_2 = 200$ Torr and Fig. 5(b) is a SAED pattern from the nanowire. Similar to the case of nanobelts, the diffraction pattern also contains two sets of diffraction spots with the zone axis of $[\bar{1}101]$ and [0001], respectively, suggesting a bicrystal
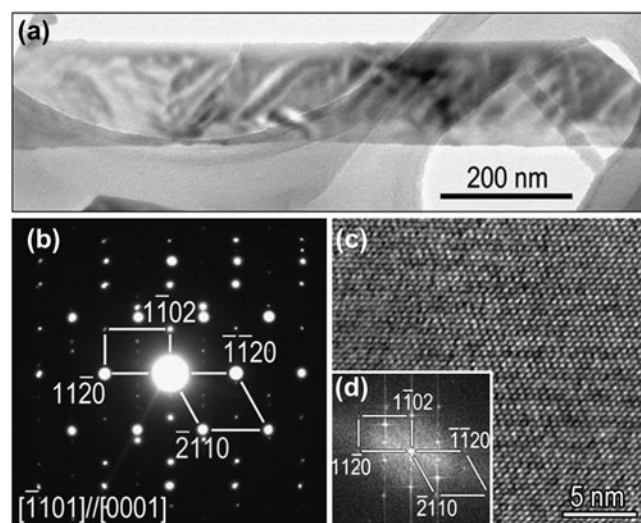


FIG. 4. (a) Bright-field (BF) TEM image of an $\alpha$-Fe$_2$O$_3$ nanobelt obtained from oxidation at $pO_2 = 0.1$ Torr; (b) SAED pattern from the nanobelt in (a); (c) HRTEM image of the nanobelt in (a); (d) a Fourier transform pattern of the HRTEM image.

structure. Figure 5(c) is a high-resolution electron microscopy image of the nanowire, which shows clearly the presence of a bicrystal boundary at middle of the nanowire. The Fourier transform patterns in Fig. 5(d) and 5(e) from the bicrystal boundary region give the same pattern
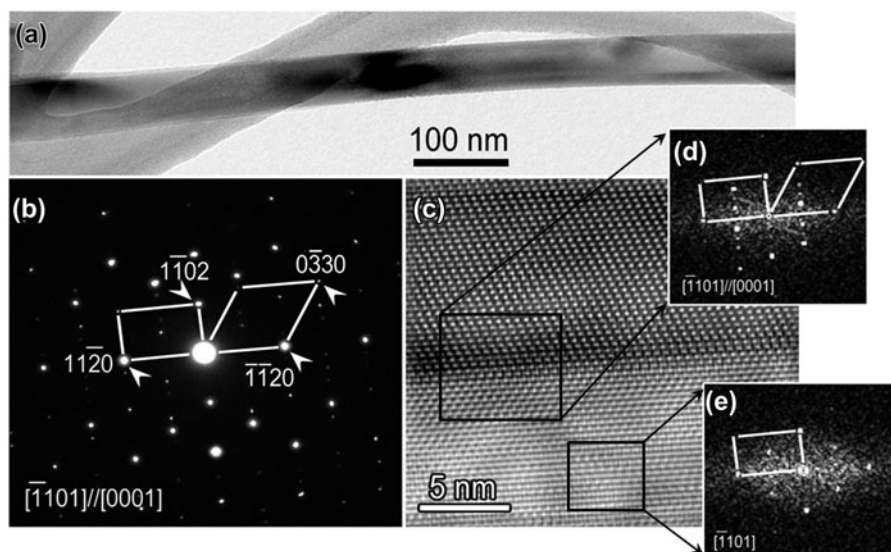
FIG. 5. (a) BF TEM image of an $\alpha$-Fe$_2$O$_3$ nanowire obtained from the oxidation at pO$_2$ = 200 Torr; (b) SAED pattern of the nanowire in (a); (c) HRTEM image of the nanowire in (a); (d, e) Fourier transform patterns from the regions indicated by the dashed boxes in the HRTEM image.
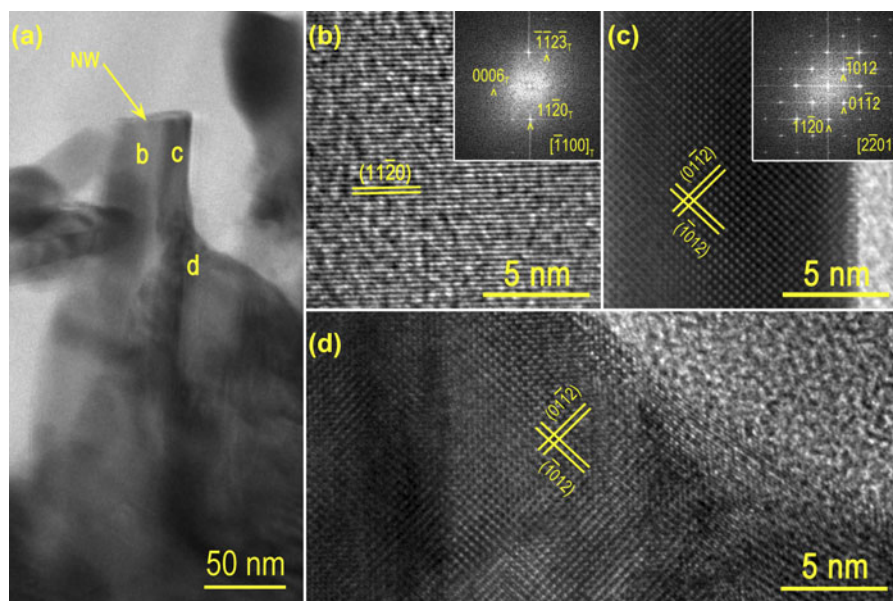


FIG. 6. (a) Cross-sectional BF TEM image showing the interface region between the nanowire root and the underlying Fe$_2$O$_3$ grain; (b) HRTEM image from the region b marked in (a), inset is its Fourier transform pattern showing the zone axis of ; (c) HRTEM image from the region c of the nanowire and the corresponding Fourier transform pattern reveals the zone axis of ; (d) HRTEM image from the region d of the underlying Fe$_2$O$_3$ grain.

as shown in Fig. 5(b), confirming the nature of the bicrystal structure of the nanowire. The length direction of the nanowire is along $[11\bar{2}0]$ as known from the electron diffraction pattern. The preferred growth direction of $[11\bar{2}0]$ for both the nanowires and nanobelts as revealed by TEM results is consistent with the XRD data, which shows that the intensity of the $(11\bar{2}0)$ peak is much stronger than other peaks (Fig. 1).

Cross-sectional TEM specimen was also made to examine the root region of nanowires formed from the

oxidation at pO$_2$ = 200 Torr. Figure 6(a) is a BF TEM image obtained from the interface region between the nanowire root and the underlying Fe$_2$O$_3$ oxide grain. It can be seen obviously that the Fe$_2$O$_3$ nanowire is formed on top of the underlying Fe$_2$O$_3$ grain, consistent with the SEM observations. Figure 6(b)–6(d) shows HRTEM images from the different regions of the nanowire and the underlying Fe$_2$O$_3$ grain as indicated in Fig. 6(a). Both the crystal lattices and Fourier transform patterns reveal that the two sides of the nanowire have different

crystal orientations due to its bicrystal structure. However, the HRTEM image [Fig. 6(d)] from the underlying $Fe_2O_3$ grain indicates that the bicrystal structure does not occur in the grain, suggesting that the formation of bicrystal structure in the nanowire is not simply a replication of the grain structure, although the bicrystal boundary in the nanowire is started from the nanowire root and then continued into the nanowire along the length direction.

## IV. DISCUSSION

Iron forms three thermodynamically stable oxides, FeO, $Fe_3O_4$, and $Fe_2O_3$. Fe can be oxidized at 600 °C to form $Fe_2O_3$/$Fe_3O_4$/FeO/Fe layered structure with FeO layer next to the metal substrate and $Fe_2O_3$ layer on the top.[49,50] This behavior of oxide layering is consistent with our experimental observations. The oxide layering is governed by the Fe and oxygen gas equilibrium conditions, whereas the growth kinetics of the multiple oxide layers is controlled by outward diffusion of Fe cations driven by chemical potential due to the many orders of magnitude in oxygen gas pressure between Fe/FeO and $Fe_2O_3$/$O_2$ interfaces. The oxide growth obeys a parabolic rate law, i.e., $x \sim (2kt)^{1/2}$, where $x$ is the oxide thickness, $k$ the rate constant, and $t$ the oxidation time.[49] Here, the rate constant $k$ is

$$k = D_{VM} V_{OX} (C''_{VM} - C'_{VM}) \quad , \qquad (1)$$

where $D_{VM}$ is the diffusion coefficient for metal cation vacancies, $V_{OX}$ is the molar volume of the oxide, and $C'_{VM}$ and $C_{VM}$ are the cation vacancy concentrations at the oxide–metal and oxide–gas interfaces, respectively.[49] The cation vacancy concentration is related to oxygen partial pressure by the equation

$$C_{VM} = \text{const} \cdot (pO_2)^{1/n} \quad , \qquad (2)$$

where $n$ is a constant depending on the charge state of the cation vacancy.[49,50] Therefore, the rate constant $k$ is proportional to $\left[ (pO''_2)^{1/n} - (pO'_2)^{1/n} \right]$, where $pO'_2$ and $pO''_2$ are the oxygen gas pressure at the oxide–gas interface and metal–oxide interface, respectively.[49] Since $pO''_2$ is usually negligible compared with $pO'_2$, the $k$ is proportional to $pO'_2$ only. Accordingly, increasing the oxygen pressure leads to larger flux of Fe cations for enhanced oxide formation, whereas a lower oxygen gas pressure results in a reduced rate of oxide formation.

We have shown previously that the driving force leading to oxide nanowire formation is related to the interfacial stresses generated by volume change accompanying the solid–solid phase transformation between the different oxide layers.[51,52] Both the formation of nanowires and nanobelts on the $Fe_2O_3$ layer can be attributed to the relaxation of the compressive stresses generated by the

volume shrinkage owing to the continuous $Fe_3O_4$ forming reaction at the $Fe_2O_3$/$Fe_3O_4$ during the oxidation of Fe. The negative stress gradient $\frac{\partial \sigma_n}{\partial s}$ from the $Fe_3O_4$/$Fe_2O_3$ interface to the free surface (i.e., $Fe_2O_3$/$O_2$ interface) results in the flux of the outward grain boundary diffusion of Fe cations through the $Fe_2O_3$ layer by

$$J_{GB} = \frac{D_{GB} \delta \Omega}{kT} \frac{\partial \sigma_n}{\partial s} \quad , \qquad (3)$$

where $D_{GB}$ is the grain boundary (GB) diffusion coefficient, $\delta$ the GB width, k Boltzmann's constant, T the absolute temperature, and $s$ is the local spatial coordinate along the diffusion path. As discussed above, increasing the oxygen gas pressure leads to enhanced $Fe_3O_4$/$Fe_2O_3$ interfacial reaction and thereby resulting in a faster rate of the generation and accumulation of compressive stress at the $Fe_3O_4$/$Fe_2O_3$ interface. This increases the stress gradient for Fe outward diffusion and promotes the delivery of Fe cations onto the top of $Fe_2O_3$ grains via combined grain boundary followed by surface diffusion, where the surface of $Fe_2O_3$ grains serves as the structure template for the nucleation of $Fe_2O_3$ nanowires. Since grains typically show different surface facets, the crystals nucleated on the grain facets grow and merge at the grain top to form a bicrystal or a multicrystal. Such a process of the nanowire formation is schematically shown in Fig. 7(a). For the lower oxygen gas pressure, the oxidation rate is reduced and the stress generation at the $Fe_3O_4$/$Fe_2O_3$ interface is correspondingly slowed, resulting in a smaller stress gradient across the $Fe_2O_3$ layer. Therefore, Fe cations are delivered only onto the grain boundary region by grain boundary diffusion and deposit on the grain surfaces near the grain boundary nadir by reacting surrounding oxygen gas. The oxide nucleated on the surface of adjacent $Fe_2O_3$ grains grows and merges
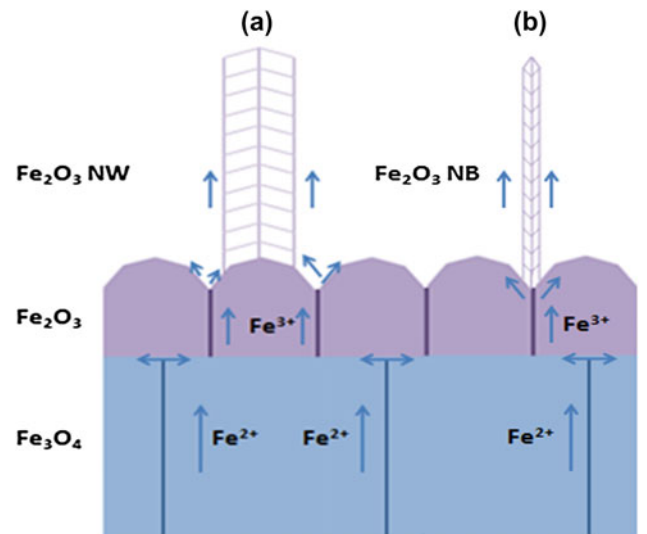


FIG. 7. Mass transport mechanisms of iron ions for the growth of α-$Fe_2O_2$ nanowire (a) and nanobelt (b).

along the grain boundary to form a bicrystal, resulting in the morphology of nanobelts, which is correlated with the geometry of the grain boundary. The process of nanobelt formation is shown schematically in Fig. 7(b).

The mechanism discussed above explains the basis why the selective formation of $Fe_2O_3$ nanowires or nanobelts can be achieved via tuning the oxygen gas pressure during the oxidation; however, it is still a challenge to develop a quantitative model to predict the dependence of the percentage of nanowires or nanobelts on the oxygen gas pressure. This is largely due to the convolution of the aforementioned kinetic and thermodynamic processes involved in the oxide nanowire/nanobelt formation including the mass transport mechanisms, interfacial reactions during the layered oxide growth, and generation/relaxation of interfacial stresses. Developing an analytic model of the nanowire/ nanobelt formation relies on the validity of some basic assumptions linking the kinetic and thermodynamic parameters and the microstructure evolution of the oxide scales to the oxygen gas pressure, which are beyond the current reach of the theories for the oxidation of metals or crystal growth.

## V. CONCLUSIONS

We have shown that the selective growth of $\alpha$-$Fe_2O_3$ nanowires and nanobelts can be achieved by simply varying oxygen gas pressure during the thermal oxidation of Fe. It is found that nanowires form on the top of underlying $Fe_2O_3$ grains, whereas nanobelts originate from the grain boundary regions of $Fe_2O_3$ grains. Our results indicate that increasing the oxygen gas pressure promotes nanowire formation while suppressing nanobelt formation. These effects are attributed to the effect of oxygen pressure on the $Fe_3O_4$/$Fe_2O_3$ interfacial reaction rate and the resulting stress-driven diffusion of Fe cations, which leads to the different surface sites for the nucleation and growth of oxide nanowires and nanobelts on the underlying $Fe_2O_3$ layer.

## ACKNOWLEDGMENT

## REFERENCES

1. K.A. Dick: A review of nanowire growth promoted by alloys and non-alloying elements with emphasis on Au-assisted III-V nanowires. *Prog. Cryst. Growth Charact. Mater.* **54**, 138 (2008).
2. J. Lu, P. Chang, and Z. Fan: Quasi-one-dimensional metal oxide materials-synthesis, properties and applications. *Mater. Sci. Eng., R* **52**, 49 (2006).
3. E. Comini, C. Baratto, G. Faglia, M. Ferroni, A. Vomiero, and G. Sberveglieri: Quasi-one-dimensional metal oxide semiconductors: Preparation, characterization and application as chemical sensors. *Prog. Mater Sci.* **54**, 1 (2009).
4. E. Park, S. Shim, R. Ha, E. Oh, B.W. Lee, and H.J. Choi: Reassembling of Ni and Pt catalyst in the vapor-liquid-solid growth of GaN nanowires. *Mater. Lett.* **65**, 2458 (2011).
5. J. Paek, M. Yamaguchi, and H. Amano: MBE-VLS growth of catalyst-free III-V axial heterostructure nanowires on (111)Si substrates. *J. Cryst. Growth* **323**, 315 (2011).
6. R. Schwertberger, D. Gold, J.P. Reithmaier, and A. Forchel: Epitaxial growth of 1.55 μm emitting InAs quantum dashes on InP-based heterostructures by GS-MBE for long-wave length laser applications. *J. Cryst. Growth* **251**, 248 (2003).
7. C. Gatel, H. Tang, C. Crestou, A. Ponchet, N. Bertru, F. Dore, and H. Folliot: Analysis by high-resolution electron microscopy of elastic strain in thick InAs layers embedded in $Ga_{0.47}In_{0.53}As$ buffers on InP(001) substrate. *Acta Mater.* **58**, 3238 (2010).
8. Z.H. Zhang, K. Sumitomo, F. Lin, H. Omi, and T. Ogino: Structure transition of Ge/Si(113) surfaces during Ge epitaxial growth. *Physica E* **24**, 157 (2004).
9. N. Motta, A. Sgarlata, R. Calarco, Q. Nguyen, J.C. Cal, F. Patella, A. Balzarotti, and M. De Crescenzi: Growth of Ge-Si(111) epitaxial layers: Intermixing, strain relaxation and island formation. *Surf. Sci.* **406**, 254 (1998).
10. H.J. Fan, A.S. Barnard, and M. Zacharias: ZnO nanowires and nanobelts: Shape selection and thermodynamic modeling. *Appl. Phys. Lett.* **90**, 143116 (2007).
11. A.S. Barnard: A thermodynamic model for the shape and stability of twinned nanostructures. *J. Phys. Chem. B* **110**, 24498 (2006).
12. A.S. Barnard, Y. Xiao, and Z. Cai: Modelling the shape and orientation of ZnO nanobelts. *Chem. Phys. Lett.* **419**, 313 (2006).
13. X.C. Jiang, T. Herricks, and Y.N. Xia: CuO nanowires can be synthesized by heating copper substrates in air. *Nano Lett.* **2**, 1333 (2002).
14. M.L. Zhong, D.C. Zeng, Z.W. Liu, H.Y. Yu, X.C. Zhong, and W.Q. Qiu: Synthesis, growth mechanism and gas-sensing properties of large-scale CuO nanowires. *Acta Mater.* **58**, 5926 (2010).
15. C.H. Xu, C.H. Woo, and S.Q. Shi: Formation of CuO nanowires on Cu foil. *Chem. Phys. Lett.* **399**, 62 (2004).
16. F. Rizzo, S.R.J. Saunders, and M. Monteiro: The oxidation behaviour of metals and alloys at high temperatures in atmospheres containing water vapour: A review. *Prog. Mater Sci.* **53**, 775 (2008).
17. Y.L. Chueh, M.W. Lai, J.Q. Liang, L.J. Chou, and Z.L. Wang: Systematic study of the growth of aligned arrays of $\alpha$-$Fe_2O_3$ and $Fe_3O_4$ nanowires by a vapor-solid process. *Adv. Funct. Mater.* **16**, 2243 (2006).
18. R. Nakamura, G. Matsubayashi, H. Tsuchiya, S. Fujimoto, and H. Nakajima: Formation of oxide nanotubes via oxidation of Fe, Cu and Ni nanowires and their structural stability: Difference in formation and shrinkage behavior of interior pores. *Acta Mater.* **57**, 5046 (2009).
19. R. Takagi: Growth of oxide whiskers on metals at high temperature. *J. Phys. Soc. Jpn.* **12**, 1212 (1957).
20. X.G. Wen, S.H. Wang, Y. Ding, Z.L. Wang, and S.H. Yang: Controlled growth of large-area, uniform, vertically aligned arrays of $\alpha$-$Fe_2O_3$ nanobelts and nanowires. *J. Phys. Chem. B* **109**, 215 (2005).
21. D.A. Voss, E.P. Butler, and T.E. Michell: The growth of hematite blades during the high temperature oxidation of iron. *Metall. Trans. A* **13A**, 929 (1982).
22. Q. Han, Y.Y. Xu, Y.Y. Fu, H. Zhang, R.M. Wang, T.M. Wang, and Z.Y. Chen: Defects and growing mechanisms of $\alpha$-$Fe_2O_3$ nanowires. *Chem. Phys. Lett.* **431**, 100 (2006).
23. Z. Dong, P. Kashkarov, and H. Zhang: Monte Carlo study for the growth of $\alpha$-$Fe_2O_3$ nanowires synthesized by thermal oxidation of iron. *Nanoscale* **2**, 524 (2010).
24. C.T. Hsieh, J.M. Chen, H.H. Lin, and H.C. Shih: Synthesis of well-ordered CuO nanofibers by a self-catalytic growth mechanism. *Appl. Phys. Lett.* **82**, 3316 (2003).

25. L.S. Huang, S.G. Yang, T. Li, B.X. Gu, Y.W. Du, Y.N. Lu, and S.Z. Shi: Preparation of large-scale cupric oxide nanowires by thermal evaporation method. *J. Cryst. Growth* **260**, 130 (2004).

26. R.A. Rapp: The high temperature oxidation of metals forming cation-diffusing scales. *Metall. Mater. Trans. B* **15**, 195 (1984).

27. G. Raynaud and R. Rapp: In situ observation of whiskers, pyramids and pits during the high-temperature oxidation of metals. *Oxid. Met.* **21**, 89 (1984).

28. P. Kofstad: *High Temperature Corrosion* (Elsevier Applied Science Publishers, Barking, UK, 1988, pp. 350–445).

29. A.M. Goncalves, L.C. Campos, A.S. Ferlauto, and R.G. Lacerda: On the growth and electrical characterization of CuO nanowires by thermal oxidation. *J. Appl. Phys.* **106**, 034303 (2009).

30. A. Kumar, A.K. Srivastava, P. Tiwari, and R.V. Nandedkar: The effect of growth parameters on the aspect ratio and number density of CuO nanorods. *J. Phys. Condens. Matter* **16**, 8531 (2004).

31. J.T. Chen, F. Zhang, J. Wang, G.A. Zhang, B.B. Miao, X.Y. Fan, D. Yan, and P.X. Yan: CuO nanowires synthesized by thermal oxidation route. *J. Alloys Compd.* **454**, 268 (2008).

32. J. Chen, L. Xu, W. Li, and X. Gou: $\alpha$-Fe$_2$O$_3$ nanotubes in gas sensor and lithium-ion battery applications. *Adv. Mater.* **17**, 582 (2005).

33. C. Wu, P. Yin, C. OuYang, and Y. Xie: Synthesis of hematite ($\alpha$-Fe$_2$O$_3$) nanorods: Diameter-size and shape effects on their applications in magnetism, lithium ion battery, and gas sensors. *J. Phys. Chem. B* **110**, 17806 (2006).

34. Y.Y. Xu, X.F. Rui, Y.Y. Fu, and H. Zhang: Magnetic properties of $\alpha$-Fe$_2$O$_3$ nanowires. *Chem. Phys. Lett.* **410**, 36 (2005).

35. L.-C. Hsu, Y.-Y. Li, C.-G. Lo, C.-W. Huang, and G. Chern: Thermal growth and magnetic characterization of $\alpha$-Fe$_2$O$_3$ nanowires. *J. Phys. D Appl. Phys.* **41**, 185003 (2008).

36. L. Suber, P. Imperatori, G. Ausanio, F. Fabbri, and H. Hofmeister: Synthesis, morphology, and magnetic characterization of iron oxide nanowires and nanotubes. *J. Phys. Chem. B* **109**, 7103 (2005).

37. L.-C. Hsu, Y.-Y. Li, and C.-Y. Hsiao: Synthesis, electrical measurement, and field emission properties of $\alpha$-Fe$_2$O$_3$ nanowires. *Nanoscale Res. Lett.* **3**, 330 (2008).

38. Y. Peng, H.L. Zhang, S.L. Pan, and H.L. Li: Magnetic properties and magnetization reversal of $\alpha$-Fe nanowires deposited in alumina film. *J. Appl. Phys.* **87**, 7405 (2000).

39. H. Wang, X. Zhang, B. Liu, H. Zhao, Y. Li, Y. Huang, and Z. Du: Synthesis and characterization of single crystal $\alpha$-Fe$_2$O$_3$ nanobelts. *Chem. Lett.* **34**, 184 (2005).

40. L.S. Zhong, J.S. Hu, H.P. Liang, A.M. Cao, W.G. Song, and L.J. Wan: Self-assembled 3D flowerlike iron oxide nanostructures and their application in water treatment. *Adv. Mater.* **18**, 2426 (2006).

41. J. Jin, S. Ohkoshi, and K. Hashimoto: Giant coercive field of nanometer-sized iron oxide. *Adv. Mater.* **16**, 48 (2004).

42. J.J. Wu, Y.L. Lee, H.H. Chiang, and D.K. Wong: Growth and magnetic properties of oriented $\alpha$-Fe$_2$O$_3$ nanorods. *J. Phys. Chem. B* **110**, 18108 (2006).

43. U. Cvelbar, Z.Q. Chen, M.K. Sunkara, and M. Mozetic: Spontaneous growth of superstructure $\alpha$-Fe$_2$O$_3$ nanowire and nanobelt arrays in reactive oxygen plasma. *Small* **4**, 1610 (2008).

44. Y.Y. Fu, J. Chen, and J. Zhang: Synthesis of Fe$_2$O$_3$ nanowires by oxidation of iron. *Chem. Phys. Lett.* **350**, 491 (2001).

45. Y.Y. Fu, R.M. Wang, J. Xu, J. Chen, Y. Yan, A.V. Narlikar, and H. Zhang: Synthesis of large arrays of aligned $\alpha$-Fe$_2$O$_3$ nanowires. *Chem. Phys. Lett.* **379**, 373 (2003).

46. A.G. Nasibulin, S. Rackauskas, H. Jiang, Y. Tian, P.R. Mudimela, S.D. Shandakov, L.I. Nasibulina, J. Sainio, and E.I. Kauppinen: Simple and rapid synthesis of $\alpha$-Fe$_2$O$_3$ nanowires under ambient conditions. *Nano Res.* **2**, 373 (2009).

47. Z.Q. Chen, U. Cvelbar, M. Mozetic, J.Q. He, and M.K. Sunkara: Long-range ordering of oxygen-vacancy planes in $\alpha$-Fe$_2$O$_3$ nanowires and nanobelts. *Chem. Mater.* **20**, 3224 (2008).

48. R.M. Wang, Y.F. Chen, Y.Y. Fu, H. Zhang, and C. Kisielowski: Bicrystalline hematite nanowires. *J. Phys. Chem. B* **109**, 12245 (2005).

49. N. Birks, G.H. Meier, and F.S. Pettit: *Introduction to the High Temperature Oxidation of Metals*, 2nd ed. (Cambridge University Press, Cambridge, United Kingdom, 2006, pp. 83–86).

50. D. Young: *High Temperature Oxidation and Corrosion of Metals* (Elsevier, Oxford, United Kingdom, 2008, pp. 85–91).

51. L. Yuan, Y.Q. Wang, R. Mema, and G.W. Zhou: Driving force and growth mechanism for spontaneous oxide nanowire formation during the thermal oxidation of metals. *Acta Mater.* **59**, 2491 (2011).

52. R. Mema, L. Yuan, Q. Du, Y.Q. Wang, and G.W. Zhou: Effect of surface stresses on CuO nanowire growth in the thermal oxidation of copper. *Chem. Phys. Lett.* **512**, 87 (2011).